

Inertial drag in granular media

Shivakumar Athani^{*} and Pierre Rognon[†]

*Particles and Grains Laboratory, School of Civil Engineering,
The University of Sydney, Sydney NSW 2006, Australia*



(Received 7 June 2019; published 3 December 2019)

Like in liquids, objects moving in granular materials experience a drag force. We investigate here whether and how an object's acceleration affects this drag force. The study is based on simulations of a canonical drag test, which involves vertically uplifting a plate through a granular packing with a prescribed acceleration pattern. Depending on the plate size, plate depth, and acceleration pattern, results provide evidence of a rate-independent regime and an inertial regime where the object acceleration strongly enhances the drag force. We introduce an elasto-inertial drag force model that captures the measured drag forces in these two regimes. The model is based on observed physical processes including a gradual, elasto-inertial mobilization of grains located above the plate. These results and analysis point out fundamental differences between mobility in granular materials upon steady and unsteady loadings.

DOI: [10.1103/PhysRevFluids.4.124302](https://doi.org/10.1103/PhysRevFluids.4.124302)

I. INTRODUCTION

Granular materials are comprised of inertial grains interacting via elastic and dissipative contacts. These interactions control the macroscopic mechanical behavior of granular packings, which is typically elasto-visco-plastic. Contact network enables finite elastic deformations, while contact sliding, opening, and formation enable large visco-plastic deformation [1].

These elementary mechanical properties underpin the ability to move large objects embedded into granular packings. In Newtonian fluids, mobility of large objects is simply described by drag force models such as Stokes and turbulent drags, which relate the speed of the object to the reaction force from the fluid. In contrast, in granular packings, the mobility of an object involves at least two distinct processes: initiating and sustaining the motion. Accordingly, models were successfully developed that establish the nature of two forces: the maximum drag force F_s an object initially at rest experiences when pulled through the packing, and the final drag force F_d it experiences afterward, while steadily moving.

Models predicting maximum drag—also called ultimate capacity—have long been established for quasistatic loadings. They are routinely used in the design of building foundations in granular soils such as sand [2–6]. For vertical uplift loadings, the maximum drag F_s is proportional to the vertical hydrostatic normal stress σ_h at the object depth:

$$F_s = N_\gamma S \sigma_h, \quad (1)$$

where S [m^2] is the surface area of the object projected in the vertical direction, and $\sigma_h = \gamma_g H$ [N/m^2] with H [m] being the object depth and γ_g [N/m^3] the unit weight of the granular packing. N_γ is a dimensionless parameter with reported values ranging from 1 to 100. Several studies have

^{*}shivakumar.athani@sydney.edu.au

[†]pierre.rognon@sydney.edu.au

shown how this parameter varies with the internal friction angle ϕ of the packing [3,7–11], the object shape [12–16], and the grain size [17–19]. The experimental method used to measure this parameter consists of uplifting the object at a constant and relatively slow velocity and monitoring the drag force during the uplift. The maximum drag F_s is then defined as the maximum value of the force opposing this motion. At low uplift velocities, the maximum drag is rate-independent [20], which is consistent with an elasto-plastic behavior of the packing.

The few reported tests performed at higher uplift velocities, including experimental results in dense sand using pipes [21,22] and plate anchors [23], revealed a linear increase in maximum drag with the uplift velocity. However, the origin of this rate-effect remains poorly understood.

Studies focusing on the final drag force F_d provide a hint toward explaining such rate effects. Final drag forces are usually measured by moving an object through a granular packing at constant speed and measuring the average force F_d needed to sustain this motion. With this method, experimental and numerical results evidence two regimes. At low speed, the drag force F_d is rate-independent and captured by a model similar to (1). Accordingly, the drag force in this regime is referred to as *frictional* drag [24–29]. At higher velocities, the drag force F_d exhibits a quadratic increase with speed that is reminiscent of a turbulent drag [30–35]. This results from the inertial forces developing when grains are moving from the front of the object to its back. This points out that grain inertia can contribute to hindering the motion of objects, and could possibly be at the origin of the rate effects evidenced on the maximum drag F_s .

The role of grain inertia on the mobility of objects in granular materials has been further evidenced under cycling loading in Ref. [36]. This study showed that an object could sustain an external force larger than F_s for a short period of time without moving. This effect was attributed to the grain inertia near the object, which hinders the object motion on short timescales. Accordingly, one could expect that an object being initially at rest and set into motion with some acceleration could possibly experience an increased maximum and final drag force, which would arise from the inertial displacement of accelerated grains in its surrounding. However, such an effect has not been evidenced to date, and there is therefore no established model to capture it.

The purpose of this paper is to measure whether and how grain inertia impedes the mobility of large objects in granular packing. With this aim, we conducted a series of elementary mobility tests using a discrete element method. Tests involve prescribing a vertical acceleration to a plate embedded into a granular packing and measuring the drag force opposing that motion. Our approach is comprised of two steps: we first empirically measure the maximum drag for different acceleration patterns, grain stiffnesses, plate sizes, and plate depths; we then develop a model capturing these measurements based on physical processes evidenced during the uplift.

The paper is organized as follows: Section II presents the simulation method and the details of the mobility tests. Sections III and IV present the measured drag forces and the model we introduce to capture them.

II. SIMULATED SYSTEM

We consider a bidimensional system comprised of a horizontal plate embedded in a packing of cohesionless and frictional grains. Figure 1(a) illustrates this configuration. The dynamics of the system is simulated by using a discrete element method. In Ref. [18], we used a similar method and system to investigate the quasistatic uplift capacity of plate anchors; this study showed that such two-dimensional (2D) numerical tests qualitatively match established experimental measurements of uplift capacity in dense sand, captured by Eq. (1).

This section briefly presents the physical parameters of the grains, the protocol of the dynamic uplift tests, and the dimensional analysis of these tests.

A. Granular material

Grains are disks of mean diameter d and mass m . A polydispersity of $d \pm 30\%$ is introduced on the grain diameter to avoid crystallization, using a uniform distribution by number within this

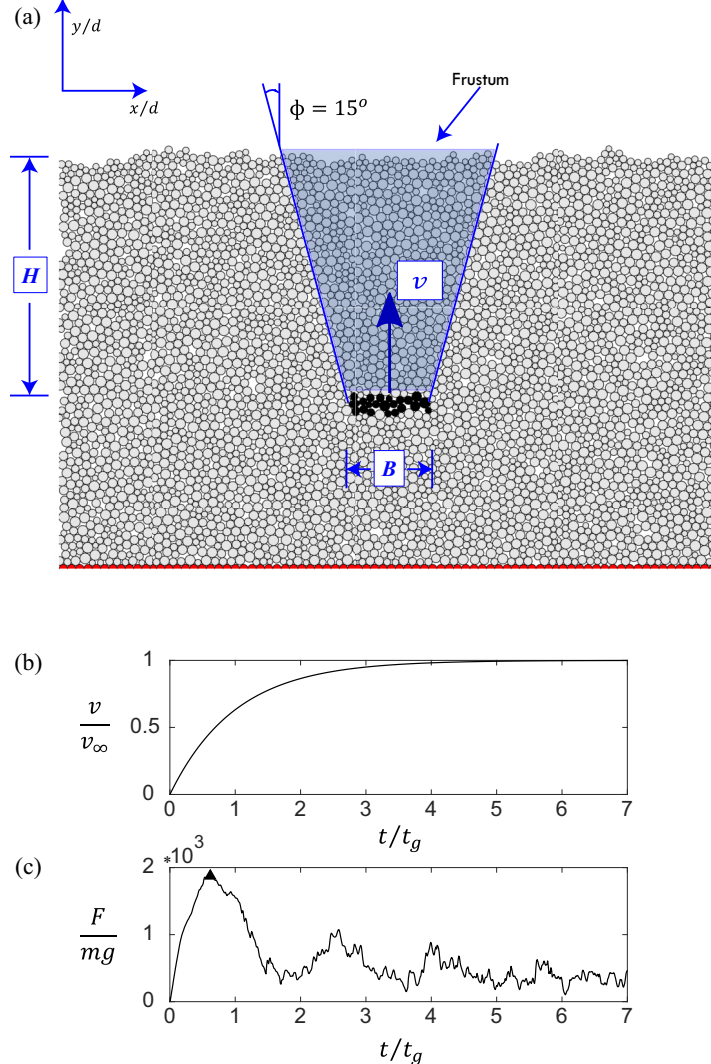


FIG. 1. Dynamic uplift tests. (a) Example of a system comprised of a plate of size B (black grains) embedded in a granular material (gray grains). The domain is bidimensional and periodic in the x direction. There is a layer of fixed grains (red grains) at $y = 0$. The system width is $8B$ and the plate is placed at a distance of at least B from the bottom. The blue area illustrates the frustum of grains being uplifted in quasistatic loadings. The weight of the grains in this zone corresponds to the maximum drag as per Eqs. (1) and (6). (b) Example of prescribed velocity of the plate, according to Eq. (2) with $\tau/t_g = 1$, showing a phase with some acceleration ($t \ll \tau$) followed by a nearly constant velocity ($t \gg \tau$). (c) Corresponding drag force F during the uplift, showing a peak force F_0 (triangle) followed by a significant decay and some fluctuations.

range. Grains are subjected to gravity. They interact with their neighbors *via* inelastic and frictional contacts characterized by a Young's modulus E , a coefficient of restitution e_r , and coefficient of friction $\mu = 0.5$.

There is no interstitial fluid in the pores or long-range interaction. Grain translation and rotation are simulated over time by using a discrete element method similar to that introduced in Refs. [18,36,37].

The plate moving through the packing is made of grains that are similar to the free grains described above. However, all plate grains move vertically at the same prescribed velocity. They do not translate horizontally or rotate. The drag force on the plate is monitored at anytime by summing up all contact forces between free grains and plate grains. This drag force therefore corresponds to the net reaction force of the granular packing and excludes the weight of the plate. In the following, $F(t)$ indicates the vertical component of this reaction force using the following convention: positive values correspond to a reaction force oriented downward. We checked that the horizontal component of the reaction force is always close to zero.

B. Dynamic uplift tests

Dynamic uplift tests involve preparing a dense and static packing of grains, placing a plate into it, and pulling the plate at a controlled velocity that can vary in time. Simulations are conducted in a domain that is periodic in the x direction. Therefore, the simulated system is an array of plates rather than a single plate. We used a domain size—corresponding to the horizontal spacing between plates—of $L = 8B$ for the tests presented in the following. We consistently observed that using larger system sizes did not affect the results, which indicates that the simulated system is representative of a single-plate behavior.

Dense packings are formed by initially placing grains at random locations in a loose configuration, without contact. Grains then settle under the action of gravity g into a denser configuration, with virtually no kinetic energy. During this preparation, grains are subjected to a background drag force of the form $\vec{f}_i^{\text{drag}} = -\xi \vec{v}_i$, where \vec{v}_i is the velocity of grain i and ξ is a drag coefficient. This background drag is introduced to limit the maximum free-fall velocity of grains to $v_{\max} = \frac{mg}{\xi}$, which restricts the build up of kinetic energy during settling. Once there is virtually no kinetic energy left in the system, the resulting packing has a porosity of about 20% and an internal friction angle of 15° . The background drag is then turned off for the uplift tests.

The plate is created within the static dense packing by selecting free grains at a desired location and tagging them as plate grains. This method avoids the creation of heterogeneities in the granular packing that would arise by either (i) placing a plate and pouring the grains or (ii) pushing a plate into a granular packing. Moreover, this method automatically produces a plate that is at mechanical equilibrium: the sum of the contact forces between free grains and plate grains balances the weight of the plate grains. The plate thus formed is not smooth: it features asperities of the order of the grain size.

The dynamic uplift tests are conducted by controlling the upward displacement of the plate using a velocity or acceleration pattern characterized by two parameters: a final uplift velocity v_∞ and an acceleration time τ . At any time t , the vertical plate acceleration and velocity along the y direction are defined by

$$v(t) = v_\infty \left(1 - e^{-\frac{t}{\tau}}\right), \quad (2)$$

$$a(t) = \frac{v_\infty}{\tau} e^{-\frac{t}{\tau}}. \quad (3)$$

The convention used for the velocity is that positive values correspond to upward motion. $t = 0$ is the beginning of the uplift test, when the plate and granular packing are at rest. These exponential functions are chosen to smoothly transition from an accelerated motion at the beginning of the test ($t \lesssim \tau$) during which the average acceleration is $\frac{v_\infty}{\tau}$, to a steady motion with a constant uplift velocity v_∞ afterward ($t \gg \tau$).

C. Dimensional analysis

The simulated system is defined by a number of geometrical and physical parameters that form elementary time, force, and length scales. In the following, we will express masses, lengths, and

TABLE I. Explored range of parameters: plate width B , embedment ratio H/B , grain coefficient of restitution e_r , Young's modulus E , final uplift velocity v_∞ , and acceleration time τ . Parameters are expressed in the system of units defined in Sec. II C. Unless otherwise specified, results shown in the following are obtained with $E = 10^4$ and $e_r = 0.5$.

B/d	H/B	e_r	$E/(mg/d^2)$	v_∞/\sqrt{gd}	τ/t_g
10	2	0.3–0.7	10^4	0.1–5	0.01–4
10	3	0.5	10^4	0.1–5	0.01–4
10	4	0.5	10^4	0.1–5	0.01–4
15	2	0.5	10^4	0.1–5	0.01–4
20	1	0.3–0.7	10^4	0.1–5	0.01–4
20	1	0.5	10^3	0.1–5	0.01–4
30	1	0.5	10^4	0.1–5	0.01–4

forces in unit grain mass m , diameter d , and weight mg , respectively. Accordingly, the unit time is $t_g = \sqrt{d/g}$. It represents the time for a grain to free fall over a distance d under the action of gravity.

The mode of loading involves two elementary timescales: the acceleration time τ , and the ultimate plate displacement timescale $t_p = d/v_\infty$. The fact that grains are inertial and elastic leads to another timescale that represents a binary collision time between two grains:

$$t_c = \sqrt{\frac{m}{Ed}}. \quad (4)$$

This time can also be interpreted as the time required for elastic waves to travel through a distance d . In the following simulations, the elastic modulus of the grains is $E = 10^4 \text{ mg}/d^2$ so that the collision time is always shorter than the gravity time: $t_c = \frac{t_g}{100}$.

The time step dt of the simulations is defined as a fraction (1/20) of the shortest timescale of the system. We checked that shorter time steps did not affect the results.

III. MEASURED PEAK FORCE F_0

Figures 1(b) and 1(c) show the results of a dynamic uplift test performed with $B/d = 10$, $H/B = 3$, $\tau/t_g = 1$, and $v_\infty = 3\sqrt{dg}$. The drag force F first increases to a maximum and then sharply decreases. Similar tests have been conducted with plates of different widths B , embedded at different depths H and with different acceleration parameters τ and v_∞ . Table I summarizes the explored range of parameters. All tests produced drag force evolutions qualitatively similar to that presented in Fig. 1(c), albeit with different values of the maximum drag force. In the following, we refer to the maximum drag force as *peak force* F_0 to distinguish it from the quasistatic maximum drag force F_s defined in Eq. (1). The relation between F_0 and F_s is

$$F_s = \lim_{v_\infty \rightarrow 0} F_0(v_\infty). \quad (5)$$

In this section, we seek to empirically establish how F_0 depends on the plate size, plate embedment, and on the acceleration parameters τ and v_∞ . The physical origin of these dependencies will be discussed in the next section.

A. Quasistatic and inertial regimes

Figure 2 shows how varying the ultimate velocity v_∞ affects the drag force. All these tests are performed with a plate size $B = 10d$, a plate depth $H = 3B$, and an acceleration time $\tau = t_g$. The only parameter varying from test to test is the ultimate uplift velocity v_∞ . Results evidence a rate-independent regime at low velocities ($v_\infty \lesssim \sqrt{gd}/10$), where the peak force F_0 does not significantly depend on the rate of pull. At larger velocities, results indicate a rate-dependent regime where the

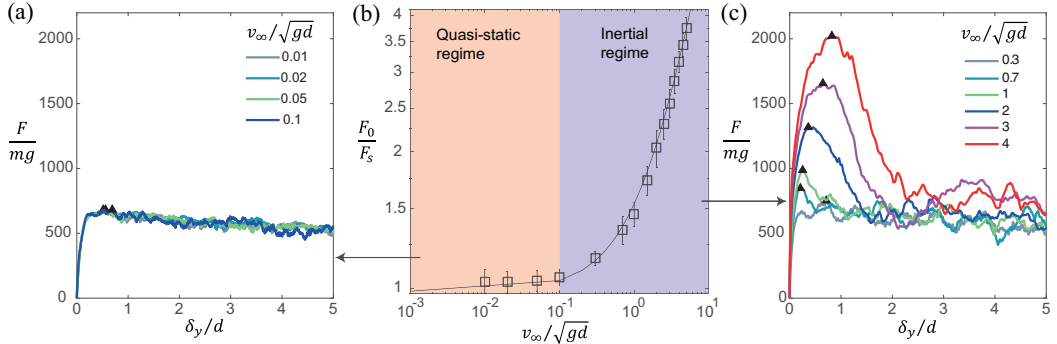


FIG. 2. Effect of the ultimate uplift velocity v_∞ on the peak drag force F_0 for a system with $B = 10d$, $H/B = 3$, and $\tau = t_g$. Examples of drag force evolution F versus plate displacement δ_y obtained (a) in the quasistatic regime ($v_\infty \lesssim \sqrt{gd}/10$) and (c) in the inertial regime ($v_\infty \gtrsim \sqrt{gd}/10$); peak forces F_0 are marked with a triangle. (b) Peak drag forces F_0 measured at different velocities v_∞ —symbols and error bars show the average and standard deviation of the peak force obtained by repeating five similar tests with different realizations of initial packing; the black line shows the best fit of the empirical model (7), using $\alpha = 390m\sqrt{g/d}$ as a fitting parameter and Eq. (6) for the quasistatic maximum drag F_s .

peak force increases approximately linearly with the ultimate velocity. We refer to these regimes as quasistatic regime and inertial regime, respectively. As in Ref. [18], we observed that the quasistatic maximum drag F_s is given by Eq. (1) with

$$N_\gamma \approx 1 + \frac{H}{B} \tan(\phi), \quad (6)$$

where $\phi \approx 15^\circ$ is the internal friction coefficient of the packing. This corresponds to the failure mode illustrated in Fig. 1(a), whereby a frustum of grains is being uplifted by the plate. The quasistatic limit of the maximum drag corresponds to the weight of this frustum of grains.

We propose to capture the maximum drag force in both the quasistatic and inertial regimes by the following linear function:

$$F_0 \approx F_s + \alpha v_\infty, \quad (7)$$

where α is a coefficient with dimensions of force per unit velocity and does not depend on v_∞ . Figure 2 shows how this function fits the measured peak forces F_0 in both the quasistatic and inertial regimes using α as a fitting parameter and fixing F_s as per Eq. (6). Figure 3 further indicates that this linear model captures the peak forces measured with different embedment and plate size, and evidences that the coefficient α depends on these parameters.

This observed linear increase in peak force with the uplift velocity is consistent with previous experimental observations in dense sand using pipes [21,22] and plate anchors [23]. In contrast, drag forces measured on objects moving at a constant and high velocity through granular packings exhibit a quadratic increase with the velocity [30–35]. This denotes a qualitative difference between the mechanisms controlling drag forces during steady and accelerated motions.

B. Effect of acceleration time τ

Figure 4 shows the effect of the acceleration time τ on the peak force for a plate of size $B = 30d$ and embedment $H = B$. The linear increase (7) is recovered for all acceleration times. However, the value of the acceleration time τ strongly influences the parameter α . For large values of τ ($\tau \gtrsim 0.1t_g$), α appears to be inversely proportional to the acceleration time:

$$\alpha \propto \tau^{-1} \quad \text{for } \tau \gtrsim 0.1t_g. \quad (8)$$

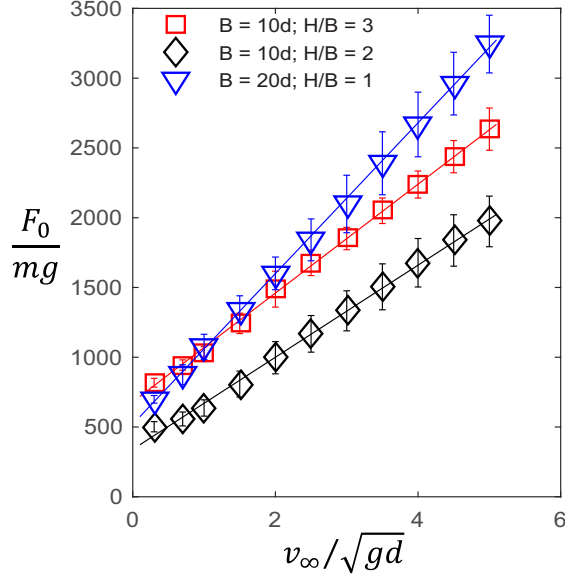


FIG. 3. Effect of the ultimate uplift velocity v_∞ on the peak force F_0 for different plate size B and plate depth H ($\tau = t_g$ in all tests). Symbols and error bars show the average and standard deviation of the peak force obtained by repeating five similar tests with different realizations of initial packing. Lines represent the best fits of the model (7) using α as a fitting parameter (best fits are obtained for $\alpha = 390, 330$, and 540 , respectively), while F_s is given by Eq. (6).

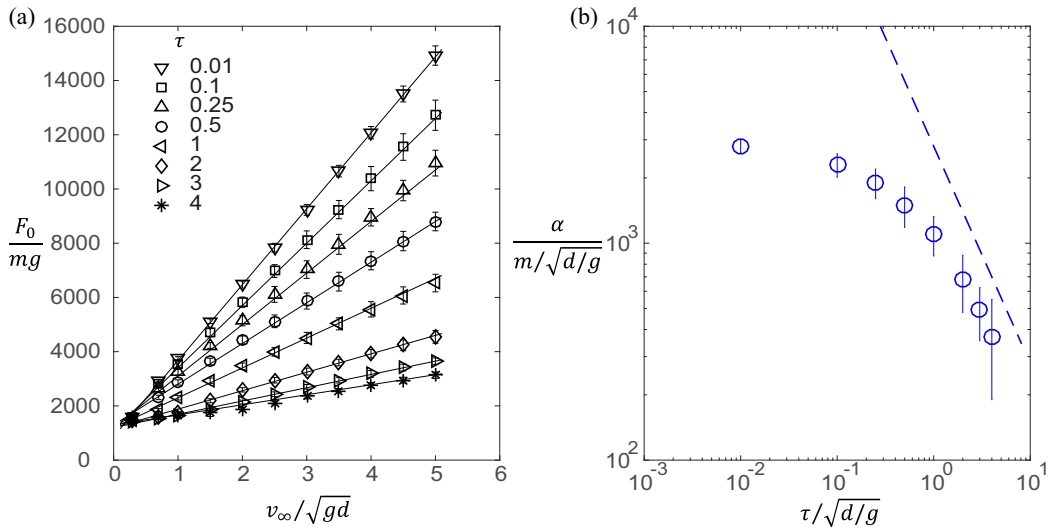


FIG. 4. Effect of the acceleration time τ on the uplift capacity F_0 for a system with $B/d = 30, H/B = 1$. (a) Peak force F_0 for different ultimate uplift velocities v_∞ and different acceleration times τ . Symbols and error bars show the average and standard deviation of F_0 obtained on a series of five tests with different realizations of the initial packing. Lines represent the best fit of Eq. (7) using α as a fitting parameter and fixing F_s as per Eq. (6). (b) Values of α obtained with this fitting procedure. The dashed line represents a power law with an exponent -1 for visual reference.

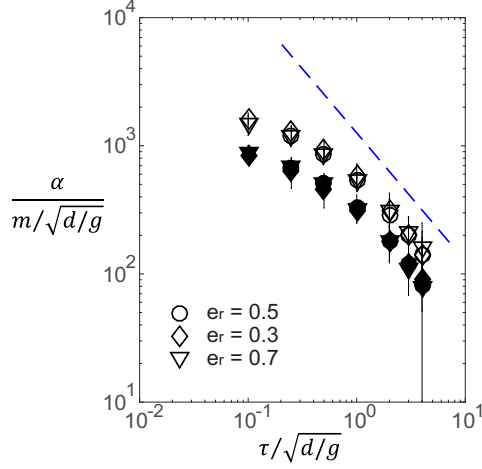


FIG. 5. Effect of the intergranular coefficient of restitution, e_r , on the peak force F_0 . Slope α measured by fitting numerical results of $F_0(v_\infty)$ by Eq. (7) following the procedure introduced in Fig. 4. Open and filled symbols correspond to systems with $B/d = 20$ and $H/B = 1$ and with $B/d = 10$ and $H/B = 2$, respectively. The dashed line represents a power law with an exponent -1 for visual reference.

In contrast, the parameter α seemingly reaches a maximum and plateaus for small acceleration times ($\tau \lesssim 0.1t_g$).

Figure 5 shows that this dependency is also observed for systems with different values of intergranular coefficient of restitution e_r , plate width B , and embedment H . The coefficient α is not affected by the value of the intergranular coefficient of restitution, which controls normal energy dissipation at the contact level.

Lastly, Fig. 6(a) shows the effect of grain stiffness on the coefficient α , by comparing systems with different values of Young's modulus E . All systems lead to a qualitatively similar function $\alpha(\tau)$, including a plateau at low values of τ and an inverse power law at large values of τ . However,

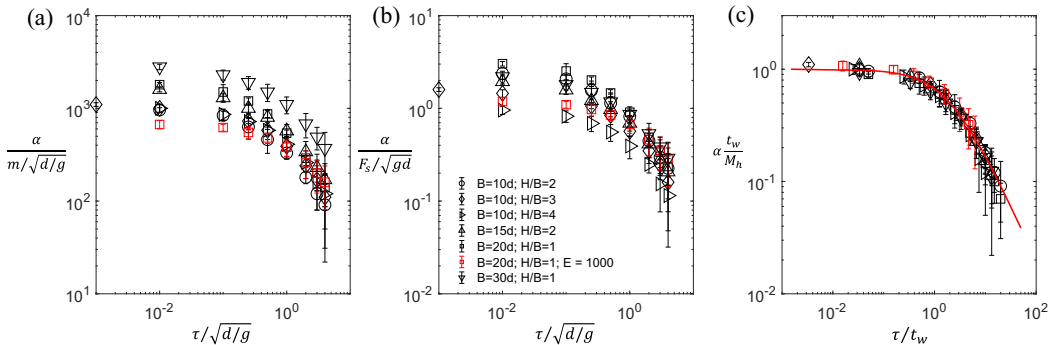


FIG. 6. Scaling of the coefficient α for different combinations of plate width B , plate depth H , acceleration times τ , and grain Young's modulus [see legend in panel (b)]. Values of α are obtained by fitting the measured values of $F_0(v_\infty)$ by Eq. (7). Black (red online) symbols correspond to grain Young's modulus $E = 10^4$ and $10^3 mg/d^2$, respectively. (a) Non-normalized values of $\alpha(\tau)$. (b) Normalization attempt using the quasistatic maximum drag force $F_s = F_0(v_\infty = 0)$ and the free-fall velocity \sqrt{gd} . (c) Successful normalization using the elastic wave propagation time t_w and the hydrostatic mass M_h defined in Eqs. (13) and (10). The red line represents the best fit of the elasto-inertial drag model defined in Eq. (20), which is obtained for $\beta = 2$.

parameters including the plate depth H , the plate width B , and the grain Young's modulus appear to quantitatively affect the value of the plateau and the value of the power-law prefactor.

IV. DYNAMIC DRAG MODEL

This section seeks to establish the physical origins of the peak force F_0 as a way to explain its dependencies with the acceleration parameters. As a starting point, we detail the established process underpinning the quasistatic maximum drag F_s . We then introduce an elasto-inertial drag model to account for the influence of the acceleration parameters v_∞ and τ .

A. Quasistatic uplift capacity

The peak force experienced by a plate being moved infinitely slowly corresponds to the weight of the grains it lifts up. Uplifted grains are not strictly limited to the column above the plate. They include grains enclosed in a frustum as illustrated in Fig. 1(a), which geometry depends on the internal friction angle of the packing. The corresponding mass M_s is (in 2D, considering a unit depth d in the third dimension)

$$M_s = M_h N_\gamma, \quad (9)$$

$$M_h = \rho B H d. \quad (10)$$

N_γ , given by Eq. (6), accounts for the shape of the frustum. In our system ($1 \leq H/B \leq 3$, $\theta \approx 15^\circ$), values of N_γ range from 1.3 to 2.1. M_h is the mass of the grains located above the plate, and ρ is the density of the packing. This process explains the quasistatic uplift force $F_s = M_s g$, which is rate-independent. While it does not account for the observed rate effects, it does point out that moving the plate requires moving some inertial grain in the packing and therefore involves some inertia.

B. Elasto-inertial drag

We infer that an accelerating plate would be resisted by two forces: the quasistatic drag mentioned above and an inertial drag F_i resulting from the grain acceleration in the packing. Accordingly, we express the peak force as

$$F_0 = F_s + F_i, \quad (11)$$

$$F_i = M^{\text{eff}} a^{\text{eff}}. \quad (12)$$

In this model, the inertial drag F_i involves an effective mass of grains being set in motion and their typical acceleration, which are denoted by M^{eff} and a^{eff} , respectively.

To establish how these two parameters may be related to the plate size, plate depth, and acceleration parameters, we consider the following elementary scenario involving the grain inertia and elasticity. Moving up the plate compresses a series of spring and mass elements. A spring element represents a grain-to-grain elastic contact with a stiffness $k = Ed$ and the mass element a grain mass m . Accordingly, accelerating the plate upward would generate an elastic wave propagating upward towards the free surface. Figure 7 illustrates this process. Each grain or contact element acts as a harmonic oscillator whose period is given by the collision time t_c . The acceleration wave thus propagates upward over a distance of one grain size d at a speed scaling like d/t_c . The time t_w for this elastic wave to reach the free surface is

$$t_w = \frac{H}{d} t_c. \quad (13)$$

When the elastic wave reaches the surface, top grains move up, freely releasing the series of springs. Accordingly, the drag force should start relaxing then, at the latest. For relatively large acceleration times ($\tau > t_w$), the plate's acceleration is sustained at a value close to $\frac{v_\infty}{\tau}$ throughout

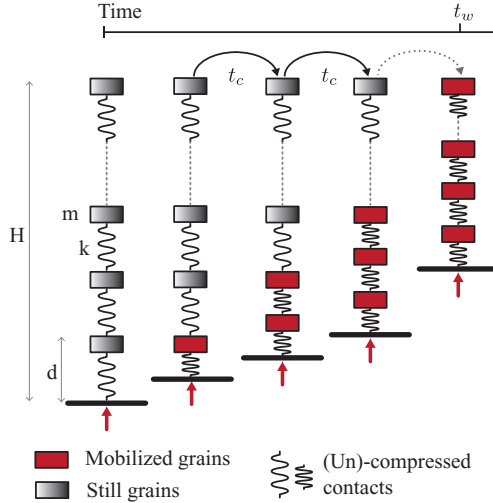


FIG. 7. Illustration of the elasto-inertial process controlling the inertial drag force. Rectangles represent layers of grains situated above the plate (black line) that are gradually mobilized as the elasto-inertial stress wave propagates toward the surface; mobilized grain's inertia yields an additional drag force.

this process. As a result, all the grains above the plate are mobilized and contribute to the inertial resistance. We therefore express the corresponding effective mass and acceleration as

$$a^{\text{eff}} = \frac{v_\infty}{\tau}, \quad (14)$$

$$M^{\text{eff}} = \beta M_h, \quad (15)$$

where β is a dimensionless constant reflecting the extent of the zone of mobilized grain above the plate, whose value is expected to be of the order of unity.

For shorter acceleration times ($\tau < t_w$), the plate stops accelerating before the elastic wave reaches the free surface. As a result, not all the grains above the plate are mobilized before it stops accelerating. If the acceleration time τ of the plate becomes shorter than the collision time ($\tau < t_c$), even the first layer of grains would not have time to move before the plate stops accelerating. The fastest the first layer of grains can be mobilized and reach a velocity of v_∞ is t_c . This defines an upper bound for the inertial drag, with an effective mass and acceleration given by

$$a^{\text{eff}} = \frac{v_\infty}{t_c}, \quad (16)$$

$$M^{\text{eff}} = M_h \frac{d}{H}. \quad (17)$$

Accordingly, the inertial force in these two regimes can be expressed as $F_i = \alpha v_\infty$ with

$$\alpha = M_h \begin{cases} \frac{\beta}{\tau}, & \text{if } \tau \gg t_w \\ \frac{1}{t_w}, & \text{if } \tau \ll t_w. \end{cases} \quad (18)$$

We propose the following interpolation between these two regimes to obtain a continuous expression for the inertial drag force:

$$F_i = \alpha v_\infty, \quad (19)$$

$$\alpha = \frac{M_h}{t_w} \frac{1}{\frac{\tau}{\beta t_w} + 1}. \quad (20)$$

C. Assessing the elasto-inertial drag model

The elasto-inertial drag model introduced in the previous section relies on a series of assumed physical processes and leads to a prediction for the scaling of the parameter α given by Eq. (20). We use here the numerical results to assess the validity of these physical processes and scaling.

1. Scaling of α

Figure 6(c) compares the measured slopes α with the model prediction in Eq. (20). When plotting the normalized slope $\alpha t_w/M_h$ as a function of the normalized acceleration time τ/t_w , all numerical data obtained for different plate sizes B , different plate embeddings H , and different grain stiffnesses E collapse onto a single curve. The prediction of the model in Eq. (20) quantitatively captures this curve in all regimes ($\tau < t_w$ and $\tau > t_w$) using a value $\beta = 2$ as sole fitting parameter. This supports the validity of the final expression of the elasto-inertial drag.

2. Partial and full mobilization of grains above the plate

Figure 8 illustrates the contact forces and the grain displacements in the granular packing when the peak force is reached. Grain displacements are analyzed *via* their average velocity and average acceleration defined by

$$v_i = \frac{x_i(t_{\text{peak}}) - x_i(t=0)}{t_{\text{peak}}}, \quad (21)$$

$$a_i = \frac{x_i(t_{\text{peak}}) - x_i(t=0)}{t_{\text{peak}}^2/2}, \quad (22)$$

where $x_i(t)$ is the position of a grain i at time t , and t_{peak} is the time at which the peak force is reached. We opted to consider these time-averaged values rather than the instantaneous velocities and accelerations because instantaneous values exhibit large fluctuations reflecting sudden and short-lived grain rearrangements.

Comparative analysis of tests performed with different acceleration times qualitatively confirm the assumptions of the elasto-inertial model:

(i) The first row in Fig. 8 illustrates a test performed with a small acceleration time of $\tau = 10^{-3}t_g$. This is shorter than that the contact time t_c , which is $10^{-2}t_g$ in all tests presented on this figure. Most of the grains above the plate have not significantly moved when the peak force is reached, except for the first layer directly above the plate. Consistently, contact forces in these layers are highly compressed. The plate velocity has reached its final value v_∞ and its averaged acceleration is lower than v_∞/τ , implying than the plate has finished accelerating before the peak force is reached ($t_{\text{peak}} > \tau$).

(ii) At the other extreme, the last row in Fig. 8 illustrates a test performed with a large acceleration time of $\tau = 2t_g$ which is larger than the wave propagation time $t_w = 0.2t_g$. All the grains located in the column above the plate, as well as some grains near this column, are mobilized when the peak force is reached. The plate velocity is lower than v_∞ and its acceleration is of the order of v_∞/τ , indicating that the plate is still accelerating when the peak force is reached ($t_{\text{peak}} < \tau$). The contact network exhibits some moderate compression from the plate to the free surface.

(iii) The two central rows in Fig. 8 show tests performed at intermediate values of τ larger than the collision time $t_c = 10^{-2}t_g$ but smaller than the wave propagation time $t_w = 0.2t_g$. They evidence that the elastic compression wave has not reached the free surface when the peak force is reached, and that only the first layers of grains that are the closest to the plate are mobilized, while the upper layers are not mobilized.

V. POSTPEAK DRAG RELAXATION

The previous section has pointed out that grain elasticity and inertia influence the maximum drag force. This section focuses on the evolution of the drag force after the maximum drag is reached.

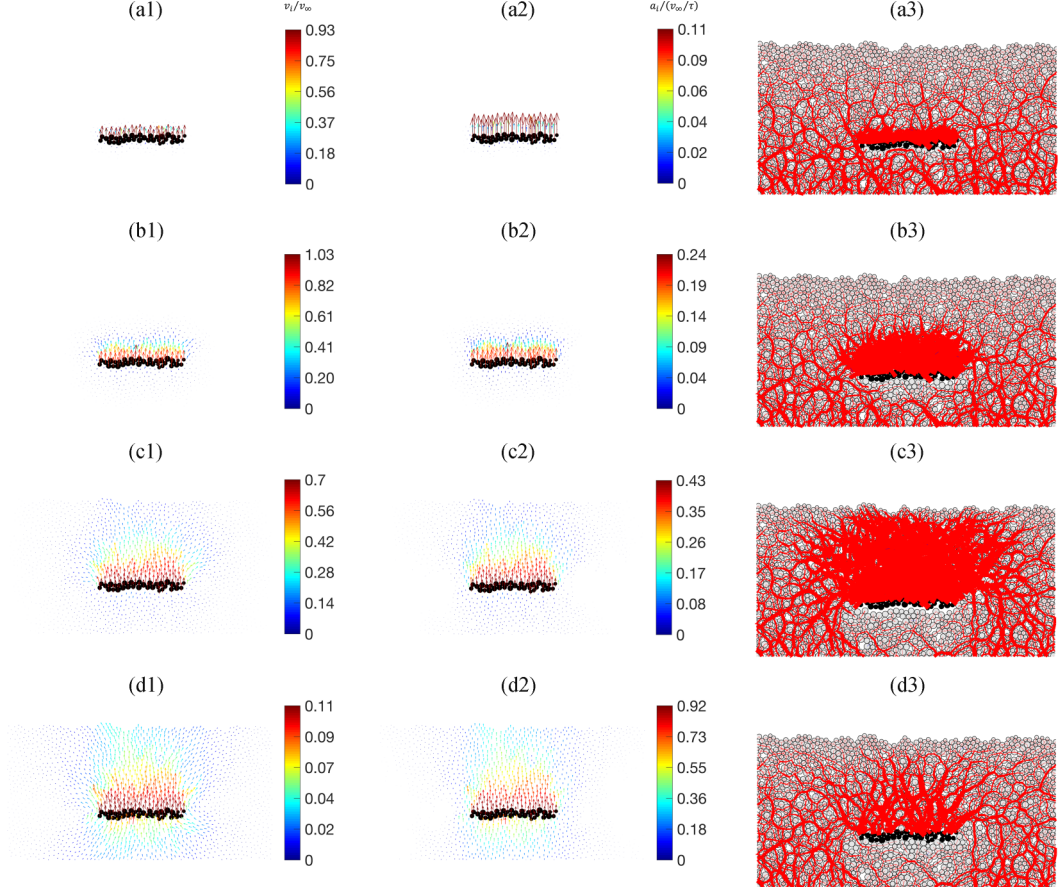


FIG. 8. Snapshots illustrating the grain mobilization and contact compression when the peak force is reached ($t = t_{\text{peak}}$). Rows (a)–(d) show uplift tests performed with $B = 20d$, $H = B$, and $v_{\infty} = 3\sqrt{gd}$ with differing acceleration times (top to bottom: $\tau/t_g = 10^{-3}, 10^{-2}, 10^{-1}$, and 2). Grain vertical displacement (left column) and vertical acceleration (middle column) averaged from $t = 0$ to t_{peak} . Normal contact force between grains at $t = t_{\text{peak}}$ (right column): red lines link grain pair in contact, with a thickness proportional to the magnitude of the normal contact force, which is purely compressive because there is no intergranular cohesion.

A. Drag force evolution after peak

Figure 9 shows examples of drag force evolution during uplift for systems subjected to different acceleration times in the range $10^{-2} \leq \tau/t_g \leq 3$. For large acceleration times ($\tau > t_g$), the drag force gradually decays after the maximum is reached, with some fluctuations. In contrast, for small acceleration times ($\tau < t_g$), the drag force sharply decays after the maximum is reached, to nearly zero.

As a way to quantify this effect, we measured the value of the drag force after the peak. At large τ , the postpeak drag force fluctuates significantly with a period of about d [Figures 9(c) and 9(d)]. We therefore consider the following average to compare tests under different conditions:

$$F_{\text{post}} = \frac{1}{4d} \int_{\delta_y=4d}^{8d} F(\delta_y) d\delta_y, \quad (23)$$

which corresponds to a small windows of displacement shortly after the maximum drag in all tests.

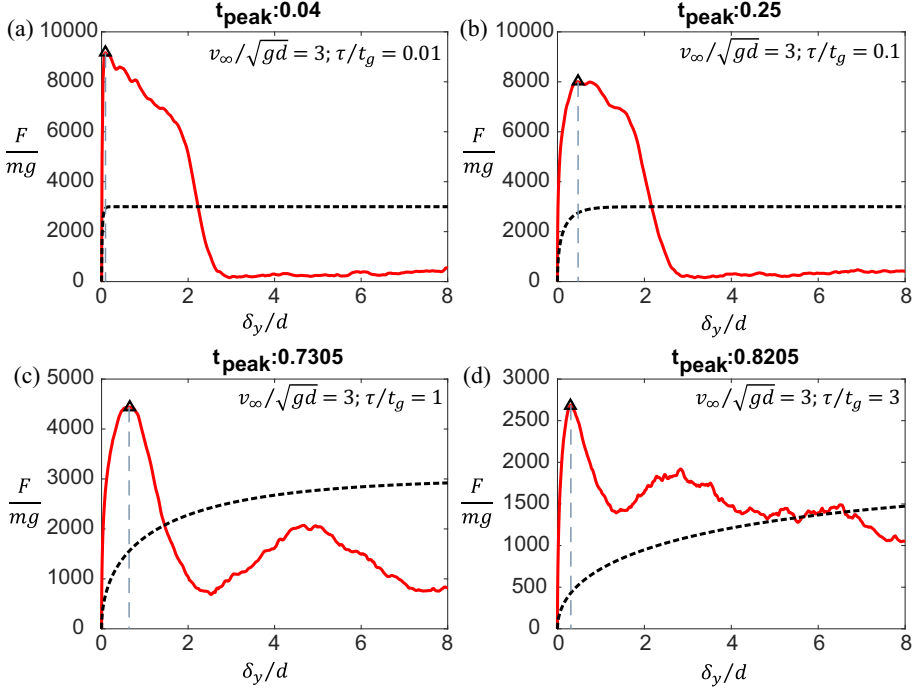


FIG. 9. Examples of drag force evolutions during uplift tests ($B = 30d$, $H/B = 1$, $v_\infty = 3\sqrt{gd}$) for different values of acceleration time τ showing different postpeak drag relaxation. Red lines denote drag forces and black dashed lines represent the prescribed plate velocity $v(\delta_y(t))$, according to Eq. (2). Markers indicate the peak force. Times t_{peak} at which the peak force is reached are indicated in units of t_g .

Figure 10 shows the values of the postpeak drag force F_{post} obtained for two plates, as a function of the ultimate velocity and acceleration time.

For long acceleration times ($\tau = 4t_g$), postpeak drag force linearly increases with the ultimate velocity v_∞ . This linear increase is similar to the peak drag force behavior. This suggests that the

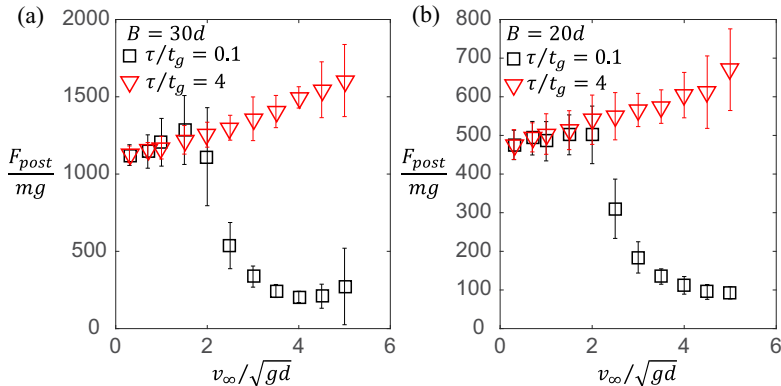


FIG. 10. Postpeak drag force F_{post} [defined in Eq. (23)] as a function of the plate ultimate velocity v_∞ . Tests shown here are performed with $H/B = 1$, with different acceleration times and different plate sizes (see legends). Symbols and error bars show the average and standard deviation of F_{post} obtained on a series of five tests with different realizations of the initial packing.

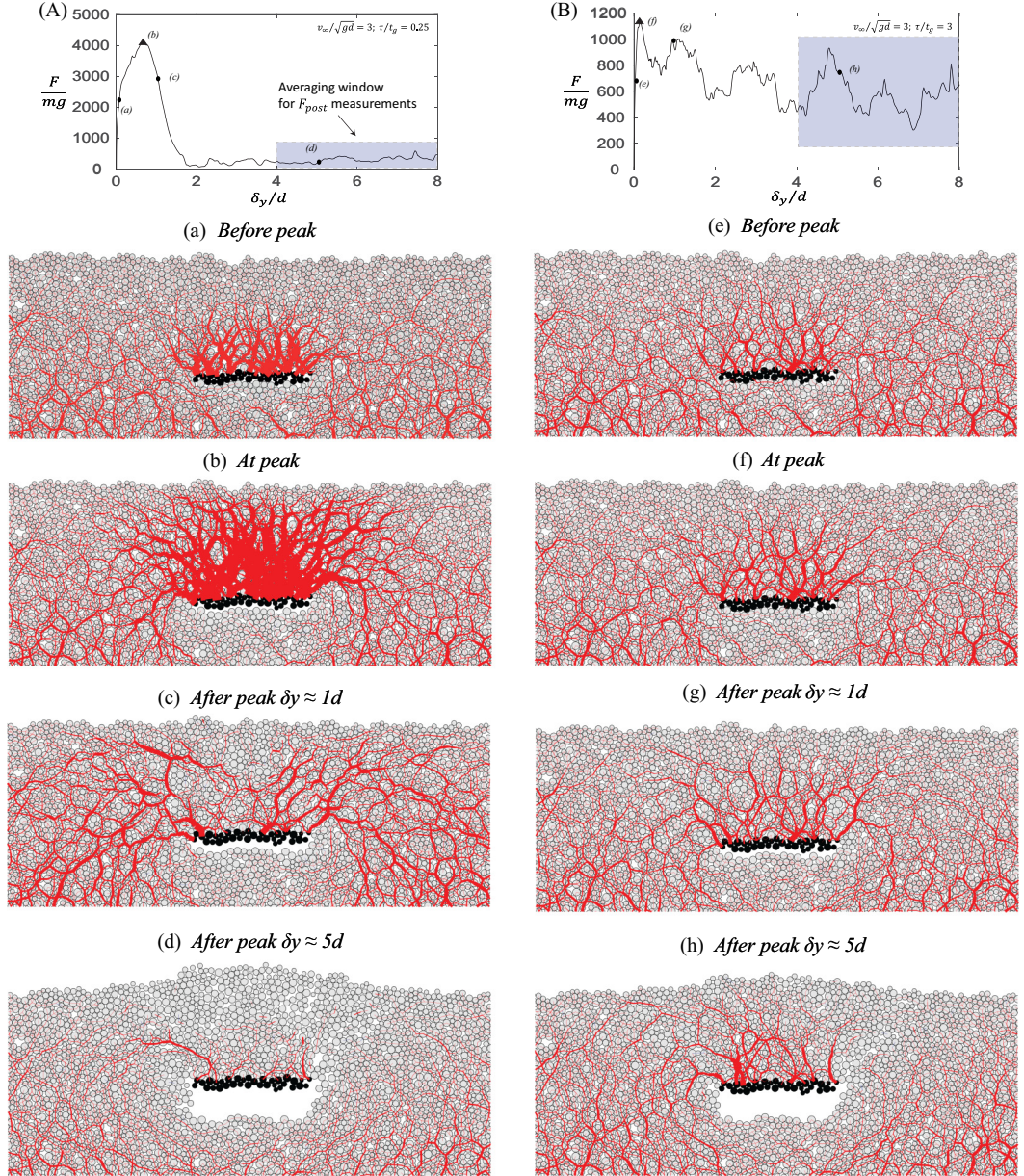


FIG. 11. Snapshot of contact network evolution during uplift. Right and left columns shows two tests performed with two different acceleration times $\tau = 0.25$ (left) and $\tau = 3t_g$ (right); in both cases, $v_\infty = 3\sqrt{gd}$, $H/d = 20$, $H/B = 1$. (A), (B) Drag force evolution, indicating when the snapshots are taken. (a)–(h) Corresponding force network: red lines denote contacts between the grains, with a width proportional to the normal contact-force magnitude.

plate is still accelerating after the maximum drag is reached, and that the postpeak drag is also enhanced by the inertia of the grains being accelerated in the packing.

For short acceleration times ($\tau = 10^{-1}t_g$), postpeak drag forces exhibit a similar linear increase with v_∞ for $v_\infty \lesssim 2\sqrt{gd}$. At higher velocities, however, the postpeak drag F_{post} drops to a small

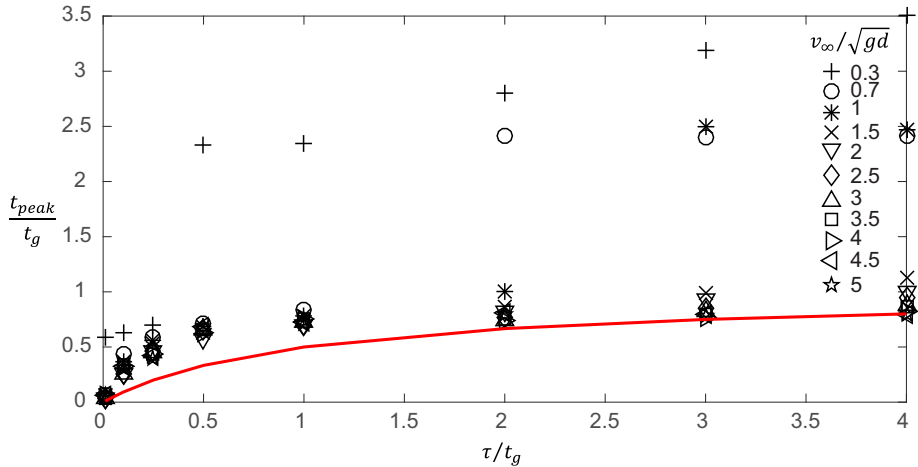


FIG. 12. Time t_{peak} at which the drag force reaches its maximum and starts relaxing ($H/B = 1, B/d = 30$). Symbols represent tests performed with different acceleration times and ultimate velocities (see legend). The red line shows the function $\frac{t_{\text{peak}}}{t_g} = \frac{\tau/t_g}{1+\tau/t_g}$ for visual reference, which behaves like $t_{\text{peak}} = \tau$ for $(\tau \ll t_g)$ and like $t_{\text{peak}} = t_g$ for $(\tau \gg t_g)$.

value. This suggests that there is a mechanism that significantly weakens the granular packing, which only develops at high ultimate velocities and short acceleration times.

Figure 11 evidences this mechanism by showing the evolution of the contact network during two uplift tests performed with a high ultimate velocity ($v_\infty = 3\sqrt{gd}$) and two different values of acceleration time ($\tau > t_g$ and $\tau < t_g$). At long acceleration time, the contact network above the plate is maintained before, during, and after the maximum drag force is reached. In contrast, the test performed with a short acceleration time evidences a loss in contact forces after the peak. The granular packing is then effectively fluidized and its resistance against the plate motion drops.

B. Mechanisms of maximum drag force relaxation

In the quasistatic regime ($v_\infty \ll \sqrt{gd}$), drag force relaxation is driven by plastic deformation in the packing that contributes to relaxing some compressed contacts. These plastic deformations take the form of grain recirculation around the plate [38–40]. The criteria $v_\infty \ll \sqrt{gd}$ can be interpreted as follows: grains can fall back under the plate by gravity quicker than the plate moves up. As a consequence, grain recirculation and its associated plastic deformations have enough time to continuously occur during the uplift.

Conversely, in the rate-dependent regime ($v_\infty \gg \sqrt{gd}$), grains do not have enough time to rearrange while the plate moves up. Figure 11 evidences the formation of a gap under the plate as it moves up and shows the upward deformation of the free surface resulting from the uplift of the packing above the plate.

This suggests that the drag force starts to relax when grains can first rearrange by recirculating under the plate under the action of gravity. This mechanism implies that the peak force is reached at $t_{\text{peak}} \approx t_g$. Figure 12 shows that this is the case for long acceleration times ($\tau > t_g$), where t_{peak} is larger than τ . In contrast, at lower acceleration times ($\tau \ll t_g$), the maximum drag force relaxation corresponds to the end of the plate acceleration ($t_{\text{peak}} \approx \tau$), and is not controlled by grain recirculation around the plate.

VI. CONCLUSIONS

This study points out that granular drag forces may be strongly affected by the acceleration of the moving object. We evidenced this effect in a series of elementary uplift tests, and we rationalized it

in terms of an elasto-inertial drag component resulting from the inertia of grains being mobilized in the packing.

The first finding is that the maximum drag force can always—at least for all the presented tests—be expressed in terms of a quasistatic component plus a dynamic component that is proportional to the final velocity of the object. This linear increase is expressed in Eq. (7). It defines the transition from a quasistatic to a rate-dependent drag regime occurring when the dynamic component becomes larger than the quasistatic component. We observed that this occurs when the ultimate plate velocity exceeds the grain free-fall velocity scale \sqrt{gd} . Consequently, we propose that the quasistatic and rate-dependent regimes correspond to whether grains have enough time to rearrange behind the moving plate to let it through the packing.

The second finding is that the dynamic drag component results from an elasto-inertial process, by which grains in the packing are gradually being accelerated when the object is set into motion, with some delay. With the considered vertical uplift configuration, a full mobilization is achieved when the plate acceleration is sustained long enough for the elasto-inertial compression wave it triggers to reach the surface. For shorter acceleration times, we observed a partial mobilization whereby only the layers closest to the plate contribute to the inertial resistance. We introduced an inertial drag model based on this process that successfully captures the measured maximum drag forces. This model is expressed in Eqs. (11) and (19).

Finally, we observed that short-lived accelerations lead to an enhanced maximum drag force, but can lead to a subsequent fluidization of the packing. As a result, the drag force may drop to nearly zero after the maximum is reached.

The scope of this study is restricted to a particular mode of loading the vertical uplift of a relatively shallow object. It is expected that similar inertial effects would arise with different modes of loading, including vertical penetration, lateral ploughing, and motions a great depth [24,31,41–43]. At constant velocity, drag forces with these loadings are similar to that measured in vertical uplift; nonetheless, the zone of mobilized grains may be qualitatively different: it may not extend to the free surface and be localized around the object. How this would affect an elasto-inertial drag component remains to be measured and understood.

- [1] B. Andreotti, Y. Forterre, and O. Pouliquen, *Granular Media: Between Fluid and Solid* (Cambridge University Press, Cambridge, 2013).
- [2] M. Randolph, S. Gourvenec, D. White, and M. Cassidy, *Offshore Geotechnical Engineering* (Spon Press, New York, 2011), Vol. 2.
- [3] B. M. Das and S. K. Shukla, *Earth Anchors* (J. Ross Publishing, 2013).
- [4] B. M. Das, *Principles of Foundation Engineering* (Cengage Learning, 2015).
- [5] J. T. Yi, S. H. Goh, F. H. Lee, and M. F. Randolph, A numerical study of cone penetration in fine-grained soils allowing for consolidation effects, *Géotechnique* **62**, 707 (2012).
- [6] N. Zhang, Numerical simulations and microscale analyses of offshore anchor-granular material systems, Ph.D. Dissertation, Oregon State University, 2018.
- [7] G. G. Meyerhof and J. I. Adams, The ultimate uplift capacity of foundations, *Can. Geotech. J.* **5**, 225 (1968).
- [8] R. K. Rowe and E. H. Davis, Behaviour of anchor plates in sand, *Geotechnique* **32**, 25 (1982).
- [9] E. J. Murray and J. D. Geddes, Uplift of anchor plates in sand, *J. Geotech. Eng.* **113**, 202 (1987).
- [10] R. S. Merifield and S. W. Sloan, The ultimate pullout capacity of anchors in frictional soils, *Can. Geotech. J.* **43**, 852 (2006).
- [11] J. Kumar and K. M. Kouzer, Vertical uplift capacity of horizontal anchors using upper bound limit analysis and finite elements, *Can. Geotech. J.* **45**, 698 (2008).
- [12] V. N. Khatri and J. Kumar, Effect of anchor width on pullout capacity of strip anchors in sand, *Can. Geotech. J.* **48**, 511 (2011).

- [13] P. Bhattacharya and J. Kumar, Pullout capacity of inclined plate anchors embedded in sand, *Can. Geotech. J.* **51**, 1365 (2014).
- [14] A. S. Dyson and P. G. Rognon, Pull-out capacity of tree root inspired anchors in shallow granular soils, *Géotechnique Lett.* **4**, 301 (2014).
- [15] H. Askari and K. Kamrin, Intrusion rheology in grains and other flowable materials, *Nat. Mater.* **15**, 1274 (2016).
- [16] J. R. Giampa, A. S. Bradshaw, H. Gerkes, R. B. Gilbert, K. G. Gavin, and V. Sivakumar, The effect of shape on the pull-out capacity of shallow plate anchors in sand, *Géotechnique* **69**, 355 (2018).
- [17] T. Sakai and T. Tanaka, Scale effect of a shallow circular anchor in dense sand, *Soils Found.* **38**, 93 (1998).
- [18] S. Athani, P. Kharel, D. Airey, and P. Rognon, Grain-size effect on uplift capacity of plate anchors in coarse granular soils, *Géotechnique Lett.* **7**, 167 (2017).
- [19] D. J. Costantino, T. J. Scheidemantel, M. B. Stone, C. Conger, K. Klein, M. Lohr, Z. Modig, and P. Schiffer, Starting to Move through a Granular Medium, *Phys. Rev. Lett.* **101**, 108001 (2008).
- [20] J.-F. Métayer, D. J. Suntrup III, C. Radin, H. L. Swinney, and M. Schröter, Shearing of frictional sphere packings, *Europhys. Lett.* **93**, 64003 (2011).
- [21] T.-W. Hsu, Rate effect on lateral soil restraint of pipelines, *Soils Found.* **33**, 159 (1993).
- [22] K. Tagaya, R. F. Scott, and H. Aboshi, Scale effect in anchor pullout test by centrifugal technique, *Soils Found.* **28**, 1 (1988).
- [23] M. E. Bychkowski, Pullout resistance of soil anchors in cohesionless soil under varying velocities by experimental methods, Master's thesis, Penn State University, 2016.
- [24] R. Albert, M. A. Pfeifer, A.-L. Barabási, and P. Schiffer, Slow Drag in a Granular Medium, *Phys. Rev. Lett.* **82**, 205 (1999).
- [25] I. Albert, P. Tegzes, B. Kahng, R. Albert, J. G. Sample, M. Pfeifer, A.-L. Barabasi, T. Vicsek, and P. Schiffer, Jamming and Fluctuations in Granular Drag, *Phys. Rev. Lett.* **84**, 5122 (2000).
- [26] I. Albert, J. G. Sample, A. J. Morss, S. Rajagopalan, A.-L. Barabási, and P. Schiffer, Granular drag on a discrete object: Shape effects on jamming, *Phys. Rev. E* **64**, 061303 (2001).
- [27] N. Gravish, P. B. Umbanhowar, and D. I. Goldman, Force and Flow Transition in Plowed Granular Media, *Phys. Rev. Lett.* **105**, 128301 (2010).
- [28] D. J. Costantino, J. Bartell, K. Scheidler, and P. Schiffer, Low-velocity granular drag in reduced gravity, *Phys. Rev. E* **83**, 011305 (2011).
- [29] Y. Ding, N. Gravish, and D. I. Goldman, Drag Induced Lift in Granular Media, *Phys. Rev. Lett.* **106**, 028001 (2011).
- [30] B. Percier, S. Manneville, J. N. McElwaine, S. W. Morris, and N. Taberlet, Lift and drag forces on an inclined plow moving over a granular surface, *Phys. Rev. E* **84**, 051302 (2011).
- [31] F. Q. Potiguara and Y. Ding, Lift and drag in intruders moving through hydrostatic granular media at high speeds, *Phys. Rev. E* **88**, 012204 (2013).
- [32] Y. Takehara, S. Fujimoto, and K. Okumura, High-velocity drag friction in dense granular media, *Europhys. Lett.* **92**, 44003 (2010).
- [33] Y. Takehara and K. Okumura, High-Velocity Drag Friction in Granular Media Near the Jamming Point, *Phys. Rev. Lett.* **112**, 148001 (2014).
- [34] T. Faug, Macroscopic force experienced by extended objects in granular flows over a very broad Froude-number range, *Eur. Phys. J. E: Soft Matter Biol. Phys.* **38**, 34 (2015).
- [35] A. Seguin, A. Lefebvre-Lepot, S. Faure, and P. Gondret, Clustering and flow around a sphere moving into a grain cloud, *Eur. Phys. J. E: Soft Matter Biol. Phys.* **39**, 63 (2016).
- [36] S. Athani and P. Rognon, Mobility in granular materials upon cyclic loading, *Granular Matter* **20**, 67 (2018).
- [37] P. G. Rognon, T. Miller, B. Metzger, and I. Einav, Long-range wall perturbations in dense granular flows, *J. Fluid Mech.* **764**, 171 (2015).
- [38] R. Candelier and O. Dauchot, Creep Motion of an Intruder within a Granular Glass Close to Jamming, *Phys. Rev. Lett.* **103**, 128001 (2009).
- [39] R. Harich, T. Darnige, E. Kolb, and E. Clément, Intruder mobility in a vibrated granular packing, *Europhys. Lett.* **96**, 54003 (2011).

- [40] E. Kolb, P. Cixous, N. Gaudouen, and T. Darnige, Rigid intruder inside a two-dimensional dense granular flow: Drag force and cavity formation, *Phys. Rev. E* **87**, 032207 (2013).
- [41] J. E. Hilton and A. Tordesillas, Drag force on a spherical intruder in a granular bed at low Froude number, *Phys. Rev. E* **88**, 062203 (2013).
- [42] F. Guillard, Y. Forterre, and O. Pouliquen, Depth-Independent Drag Force Induced by Stirring in Granular Media, *Phys. Rev. Lett.* **110**, 138303 (2013).
- [43] A. Seguin, Hysteresis of the drag force of an intruder moving into a granular medium, *Eur. Phys. J. E: Soft Matter Biol. Phys.* **42**, 13 (2019).